Available online at www.sciencedirect.com

ScienceDirect

International Journal of Heat and Mass Transfer 50 (2007) 833–846

International Journal of HEAT and MASS TRANSFER

www.elsevier.com/locate/ijhmt

Heat and mass transfer in gas metal arc welding. Part I: The arc

J. Hu [1], H.L. Tsai *

Department of Mechanical and Aerospace Engineering, University of Missouri–Rolla, 1870 Miner Circle, Rolla, MO 65409, United States

Received 18 January 2006; received in revised form 22 August 2006
Available online 24 October 2006

Abstract

A unified comprehensive model was developed to simulate the transport phenomena occurring during the gas metal arc welding process. An interactive coupling between arc plasma; melting of the electrode; droplet formation, detachment, transfer, and impingement onto the workpiece; and weld pool dynamics all were considered. Based on the unified model, a thorough investigation of the plasma arc characteristics during the gas metal arc welding process was conducted. It was found that the droplet transfer and the deformed weld pool surface have significant effects on the transient distributions of current density, arc temperature and arc pressure, which were normally assumed to be constant Gaussian profiles.

Keywords: GMAW; Arc plasma; Heat transfer; Fluid flow

1. Introduction

Gas metal arc welding (GMAW) is an arc welding process that uses a plasma arc between a continuous, consumable filler-metal electrode and the weld pool, as shown in Fig. 1. The high temperature plasma arc melts the electrode and forms a droplet at the electrode tip. The droplet is detached and transferred in the arc to the workpiece. A weld pool forms under the influences of the arc plasma and the periodical impingement of droplets. The formation of droplet, the transfer of droplet in the arc, and the dynamics of weld pool are governed by the balance of forces and the heat transfer inside the droplet or within the weld pool and the heat transferred from the arc plasma. The forces include gravity, surface tension, electromagnetic force, arc pressure, and plasma shear stress. The balance of the forces at the droplet determines the shape, volume, and frequency of the droplet detachment and the droplet acceleration after the detachment. The weld pool dynamics are not only influenced by the balance of forces acting on it, but are also affected by droplet impingement. The heat transfer within the droplet and weld pool includes Ohmic heating, conduction, and convection. The heat transferred from the arc plasma includes conduction and heat through thermal effect at the surface of the anode and cathode. Most of these forces and heat flux terms change as a function of time. They depend on the instantaneous electrode and weld pool configurations; the droplet position; the current density distribution within the arc, the electrode, and the weld pool; the thermophysical properties and the fluid flow of the plasma; and the energy balance of the plasma, the electrode, and the workpiece.

Modeling the heat transfer and fluid flow in the arc plasma for GTAW [1–18] has been well documented, but very few research articles can be found for GMAW. Mckelliget and Szekely [1], Choo et al. [2] and Goodarzi et al. [3] have simulated the arc column by assuming the current density distribution at the cathode surface in GTAW. Fan et al. [4,5] used fixed temperature boundary conditions at the cathode tip to calculate the arc column in GTAW. Zhu et al. [6] developed a unified model to simulate the

---

* Corresponding author. Tel.: +1 573 341 4945; fax: +1 573 341 4607. *E-mail address:* tsai@umr.edu (H.L. Tsai).

[1] Current address: Department of Mechanical Engineering, University of Bridgeport, Bridgeport, CT 06604, United States.

0017-9310/$ - see front matter © 2006 Elsevier Ltd. All rights reserved.
doi:10.1016/j.ijheatmasstransfer.2006.08.025

Nomenclature

A_v	constant, defined in Eq. (19)
B_θ	self-induced azimuthal magnetic field
c	specific heat
C	coefficient, defined in Eq. (11)
c_1	permeability coefficient, defined in Eq. (10)
d	dendrite arm spacing
e	electronic charge
F	volume of fluid function
f	mass fraction
g	volume fraction or gravitational acceleration
h	enthalpy
H	latent heat of fusion
H_{ev}	latent heat of vaporization
I	welding current
J_{a}	anode current density
J_{r}	radial current density
J_{z}	axial current density
k	thermal conductivity
K	permeability, defined in Eq. (10)
k_{b}	Stefan–Boltzmann constant
k_{eff}	effective thermal conductivity at arc-metal interface
$\vec{n}$	vector normal to the local free surface
p	pressure
P_{atm}	atmospheric pressure
p_{s}	surface tension pressure
Q	shielding gas flow rate
q_{ev}	evaporation mass rate of metal vapor
r-z	cylindrical coordinate system
R	gas constant
R_{n}	internal radius of the shielding gas nozzle
R_{w}	radius of the electrode
$\vec{s}$	vector tangential to the local free surface
S_{a}	anode sheath energy heat flux for the metal
S_{ap}	anode sheath energy heat flux for the arc plasma
S_{c}	cathode sheath energy heat flux for the metal
S_{cp}	cathode sheath energy heat flux for the arc plasma
S_{R}	radiation heat loss

t	time
T	temperature
T_{arc}	arc plasma temperature close to the anode and cathode
$T_{\mathrm{a}}, T_{\mathrm{c}}$	anode, cathode surface temperature
T_{l}	liquidus temperature
T_{s}	solidus temperature
T_∞	ambient temperature
u	velocity in r-direction
v	velocity in z-direction
$\boldsymbol{V}$	velocity vector
$\boldsymbol{V}_{\mathrm{r}}$	relative velocity vector ($V_{\mathrm{l}} - V_{\mathrm{s}}$)
V_{w}	wire feed rate
W	melt evaporation rate

Greek symbols

β_{T}	thermal expansion coefficient
γ	surface tension coefficient
$\partial\gamma/\partial T$	surface tension temperature gradient
ε	surface radiation emissivity
κ	free surface curvature
μ_{l}	dynamic viscosity
μ_0	magnetic permeability
ϕ	electric potential
ϕ_{w}	work function of the anode material
σ_{e}	electrical conductivity
ρ	density
τ_{ps}	plasma shear stress
τ_{Ms}	Marangoni shear stress
δ	length of the anode or cathode sheath
Δt	time interval

Subscripts

0	initial value
l	liquid phase
r	relative to solid phase velocity
s	solid phase
w	wire

arc column, the cathode and the cathode sheath in GTAW. Lowke et al. [7,8] simplified the unified model to treat the electrode in a special way at the cathode surface to account for electrode effects [7] or omit the electrode sheath [8]. The simplified models [7,8] reduced the computation time to 1% of the original unified model and gave fair results in agreement with experimental data when 0.005–0.01 cm mesh size around the cathode tip was chosen. These simplified models have been used and further developed by many researchers [9–18] to calculate the heat transfer and fluid flow in the arc column.

Both GTAW and GMAW have a plasma arc struck between an electrode and a workpiece. Even though the GTAW has an inert tungsten cathode as the electrode and the electrode of GMAW is a melting metal and usually set as the anode, the GTAW arc model can be adopted to model the GMAW arc. Jonsson [19] adopted the GTAW arc model of Mckelliget and Szekely [1] to calculate the arc column by assuming a current density distribution at the cathode spot. Zhu et al. [20] calculated the anode temperature profile by incorporating the simplified arc model of Lowke et al. [8] into a one-dimensional conduction model of the moving electrode in GMAW. The heat input to the electrode was estimated from the arc plasma, and the 'molten' metal was discarded when its temperature reached the melting point. Haidar and Lowke [21] and Haidar [22]

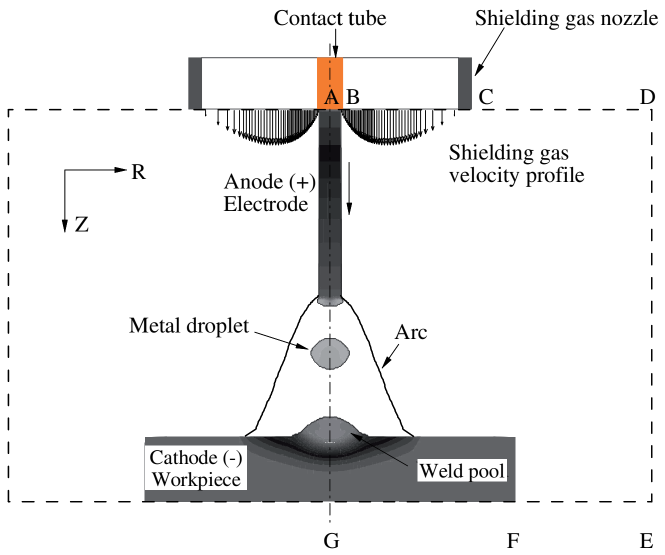

Fig. 1. A schematic representation of a GMAW system including the electrode, the arc, and the weld pool (not to scale).

extended the simplified arc model of Lowke et al. [8] to simulate the droplet formation in GMAW. They were the first to simulate the dynamic interaction of the arc plasma and the droplet. Haidar [13,23,24] further developed this GMAW model to take into account the sheath effect at the anode surface. However, the droplet was eliminated immediately when it was detached from the electrode tip. The weld pool dynamics was also neglected and the workpiece was treated as a flat plate. The fluid flow in the weld pool was not calculated and only conduction was considered. Zhu et al. [25] and Fan and Kovacevic [26] have developed models to simulate the arc column, droplet formation, detachment, transfer and impingement onto the workpiece and the weld pool dynamics. However, the simulated arc plasma distributions matched both the experimental results [27–31] and the simulation results from aforementioned arc models [1–24] poorly. From the simulated fluid flow within the droplets in Ref. [25], the coupling of the arc plasma and the droplets seemed to be poor as the droplets showed very little sign of being subjected to the electromagnetic force, arc pressure, and plasma shear force. The arc plasma flow in Ref. [26] could not push the detached droplets down and an empirical formulation was used to calculate the plasma drag force.

In almost all of the aforementioned studies, the arc plasma was considered to be independent of electrode melting, droplet generation and transfer, or weld pool dynamics. However, in reality, the surface of the weld pool is highly deformable, and the profile of the electrode changes rapidly. Also, when there are droplets between the electrode tip and the surface of the welding pool, the flow of arc plasma can be dramatically distorted. In this article, a mathematical model employing the volume of fluid (VOF) technique and the continuum formulation is developed to simulate the coupled transport phenomena including the generation and changes of the arc plasma; the electrode melting; the droplet formation, detachment, transfer, and impingement onto the workpiece; and the dynamics of the weld pool. This paper will focus on presenting the results of the plasma arc. A second paper on the electrode melting; droplet formation, transfer, detachment and impingement onto the base metal; and the dynamics of the welding pool is presented separately.

2. Mathematical model

2.1. Governing equations

Fig. 1 is a schematic sketch of a stationary axisymmetric GMAW system. In this system, a constant current is applied to the electrode through the contact tube at the top of the computational domain. An arc plasma is struck between the electrode and the workpiece. The electrode is continuously fed downward and then melted at the tip by the high temperature arc. Droplets are formed at the molten electrode tip, and are then detached and transferred to the workpiece. A weld pool is formed by the continuous impingement of droplets and dynamic interaction with the high temperature and high pressure arc plasma at the workpiece. Inert shielding gas is provided through the shielding gas nozzle to prevent the molten metal from oxidation.

The computational domain has an anode region, an arc region and a cathode region. For GMAW, the anode region is the electrode, and the cathode region is the workpiece. The anode sheath region and the cathode sheath region have been omitted and treated as special boundary conditions in this model for computational simplification [7,8]. The differential equations governing the arc, the electrode, and the workpiece can be put into a single set. The differential equations governing the conservation of mass, momentum, and energy based on the continuum formulation given by Diao and Tsai [32] are employed in the present study, and the current continuity equation is used to calculate the current density distribution. The equations are given below:

Mass continuity

$$\frac{\partial}{\partial t}(\rho) + \nabla \cdot (\rho \boldsymbol{V}) = 0 \tag{1}$$

Momentum

$$\begin{aligned}\frac{\partial}{\partial t}(\rho u) + \nabla \cdot (\rho \boldsymbol{V} u) &= \nabla \cdot \left(\mu_{\mathrm{l}} \frac{\rho}{\rho_{\mathrm{l}}} \nabla u\right) - \frac{\partial p}{\partial r} - \frac{\mu_{\mathrm{l}}}{K} \frac{\rho}{\rho_{\mathrm{l}}}(u - u_{\mathrm{s}}) \\ &\quad - \frac{C\rho^2}{K^{1/2}\rho_{\mathrm{l}}}|u - u_{\mathrm{s}}|(u - u_{\mathrm{s}}) - \nabla \cdot (\rho f_{\mathrm{s}} f_{\mathrm{l}} \boldsymbol{V}_{\mathrm{r}} u_{\mathrm{r}}) - J_z \times B_\theta\end{aligned} \tag{2}$$

$$\frac{\partial}{\partial t}(\rho v)+\nabla\cdot(\rho \boldsymbol{V} v) = \nabla\cdot\left(\mu_1\frac{\rho}{\rho_1}\nabla v\right)-\frac{\partial p}{\partial z}-\frac{\mu_1}{K}\frac{\rho}{\rho_1}(v-v_s) - \frac{C\rho^2}{K^{1/2}\rho_1}|v-v_s|(v-v_s)-\nabla\cdot(\rho f_s f_1 V_r v_r) + \rho g\beta_T(T-T_0)+J_r\times B_\theta \tag{3}$$

Energy

$$\frac{\partial}{\partial t}(\rho h)+\nabla\cdot(\rho \boldsymbol{V} h) = \nabla\cdot\left(\frac{k}{c_s}\nabla h\right)+\nabla\cdot\left(\frac{k}{c_s}\nabla(h_s-h)\right) - \nabla\cdot(\rho(\boldsymbol{V}-\boldsymbol{V}_s)(h_1-h))-\Delta H\frac{\partial f_1}{\partial t}+\frac{J_r^2+J_z^2}{\sigma_e} - S_R+\frac{5k_b}{e}\left(\frac{J_r}{c_s}\frac{\partial h}{\partial r}+\frac{J_z}{c_s}\frac{\partial h}{\partial z}\right) \tag{4}$$

Current continuity

$$\nabla^2\phi=\frac{1}{r}\frac{\partial}{\partial r}\left(r\frac{\partial\phi}{\partial r}\right)+\frac{\partial^2\phi}{\partial z^2}=0 \tag{5}$$

Ohm's law

$$J_r=-\sigma_e\frac{\partial\phi}{\partial r},\quad J_z=-\sigma_e\frac{\partial\phi}{\partial z} \tag{6}$$

Maxwell's equation

$$B_\theta=\frac{\mu_0}{r}\int_0^r J_z r\,\mathrm{d}r \tag{7}$$

In Eqs. (1)–(4), u and v are the velocities in the r and z directions, respectively. $\boldsymbol{V}_r=\boldsymbol{V}_1-\boldsymbol{V}_s$ is the relative velocity vector between the liquid phase and the solid phase in the mushy zone. The subscripts s and l refer to the solid and liquid phases, respectively, and the subscript 0 represents the initial condition. f is the mass fraction of the liquid or solid; K is the permeability function; C is the inertial coefficient; p is the pressure; T is the temperature; h is the enthalpy; Φ is the electrical potential; ρ is the density; μ is the viscosity; k is the thermal conductivity; g is the gravitational acceleration; β_T is the thermal expansion coefficient; c is the specific heat; σ_e is the electrical conductivity; J_r and J_z are current densities, in the respective r and z directions; B_θ is the self-induced electromagnetic field; S_R is the radiation heat loss; μ_0 is the magnetic permeability; k_b is the Stefan–Boltzmann constant; and e is the electronic charge.

The third and fourth terms on the right-hand side of Eqs. (2) and (3) represent the respective first- and second-order drag forces for the flow in the mushy zone. The fifth term on the right-hand side of Eqs. (2) and (3) represents an interaction between the solid and the liquid phases. The second term on the right-hand side of Eq. (4) represents the net Fourier diffusion flux. The third term represents the energy flux associated with the relative phase motion, and the forth term is used to consider the latent heat of fusion. All the terms mentioned in this paragraph are zero, except in the mushy zone. When Eqs. (2)–(4) are used to calculate the arc plasma, these terms associated with the mushy zone are set to zero and all the thermal physical properties are replaced with those of the arc plasma. In the present study, the solid phase velocity is assumed to be zero due to a relative small weld pool (as compared to, for example, a casting), concentrated arc heat, and rapid solidification of the weld pool after the arc is turned off.

The second-to-last term on the right-hand side of Eq. (3) is the thermal expansion term. The last term of Eqs. (2) and (3) is the electromagnetic force term. The last three terms in Eq. (4) are Ohmic heating, radiation loss, and energy transfer due to electron flow, respectively [6–9]. Electron enthalpy flow has been omitted in the energy equation due to its strong cooling effect in the cathode region and heating effect in the anode region [6–9,21–23].

Continuum density, specific heat, thermal conductivity, solid mass fraction, liquid mass fraction, velocity, and enthalpy are defined as follows:

$$\rho=g_s\rho_s+g_1\rho_1, c=f_s c_s+f_1 c_1, k=g_s k_s+g_1 k_1$$
$$f_s=\frac{g_s\rho_s}{\rho}, f_1=\frac{g_1\rho_1}{\rho} \tag{8}$$
$$\boldsymbol{V}=f_s\boldsymbol{V}_s+f_1\boldsymbol{V}_1, h=h_s f_s+h_1 f_1$$

Assuming constant phase specific heats, the phase enthalpy for the solid and liquid can be expressed as

$$h_s=c_s T, h_1=c_1 T+(c_s-c_1)T_s+H \tag{9}$$

where H is the latent heat of fusion for the alloy.

The assumption of permeability function in the mushy zone requires consideration of the growth morphology specific to the alloy under study. In the present study, the permeability function analogous to fluid flow in porous media is assumed, employing the Carman–Kozeny equation [33,34]

$$K=\frac{g_1^3}{c_1(1-g_1)^2}, c_1=\frac{180}{d^2} \tag{10}$$

where d is proportional to the dendrite dimension, which is assumed to be a constant and is on the order of 10^{-2} cm The inertial coefficient, C, can be calculated from [35]

$$C=0.13g_1^{-3/2} \tag{11}$$

2.2. Arc region

In the arc region, the plasma is assumed to be in local thermodynamic equilibrium (LTE) [8], implying the electron and the heavy particle temperatures are equal. On this basis, the plasma properties, including enthalpy, specific heat, density, viscosity, thermal conductivity and electrical conductivity, are determined from an equilibrium composition calculation [8,36]. It is noted that the metal vaporized from the metal surface may influence plasma material properties, but this effect is omitted in the present study. It is also assumed that the plasma is optically thin, thus the radiation may be modeled in an approximate manner by defining a radiation heat loss per unit volume as indicated by S_R in Eq. (4) [8,36].

2.3. Metal region (electrode, droplet and workpiece)

In this model, the anode region and cathode region change their shapes with time. Together with detached droplets in the arc, they consist of the metal region, which is occupied by metal. The temperature distribution within the metal region is at an energy balance of conduction, Ohmic heating, and convection in the metal and the heat transferred from the arc plasma. Considerations are also given to energy gains and losses due to latent heat resulting from melting and solidification at the solid–liquid interface. Changes in the shape of the electrode tip and the weld pool surface result in changes in the current distribution, the heat generated due to Ohmic heating, and the heat transferred from the arc to the metal surface.

2.4. Tracking of solid–liquid interface

The solid/liquid phase-change boundary is handled by the continuum model [32]. The third, fourth, and fifth terms on the right-hand-side of Eqs. (2) and (3) vanish at the solid phase because $u = u_s = v = v_s = 0$ and $f_l = 0$. For the liquid region, since K goes to infinity due to $g_l = 1$ in Eq. (7) and $f_s = 0$, all the aforementioned terms also vanish. These terms are only valid in the mushy zone, where $0 < f_l < 1$ and $0 < f_s < 1$. Therefore, there is no need to explicitly track the phase-change boundaries, and the liquid region, mushy zone, and solid region are all calculated by the same Eqs. (2) and (3). During the fusion and solidification processes, the latent heat is absorbed or released in the mushy zone, which is handled through the use of enthalpy defined in Eq. (9).

2.5. Tracking of free surfaces

Precise tracking of the free surface of the droplet and the welding pool are essential to correctly predicting the shape of the droplet and the weld pool as a function of time. The algorithm of volume-of-fluid (VOF) is used to track the moving free surface [37]. The fluid configuration is defined by a volume of fluid function,$F(r,z,t)$, which tracks the location of the free surface. This function represents the volume of fluid per unit volume and satisfies the following conservation equation

$$\frac{dF}{dt} = \frac{\partial F}{\partial t} + (\boldsymbol{V} \cdot \nabla)F = 0 \tag{12}$$

When averaged over the cells of a computing mesh, the average value of F in a cell is equal to the fractional volume of the cell occupied by the metal. A unit value of F corresponds to a cell full of metal, whereas a zero value indicates the cell contains no metal. Cells with F values between zero and one are partially filled with metal.

2.6. Forces at the arc plasma and metal interface

The molten part of the metal is subjected to body forces such as gravity and electromagnetic force. It is also subjected to surface forces such as surface tension due to surface curvature, Marangoni shear stress due to temperature difference, and arc plasma shear stress and arc pressure at the arc plasma and metal interface.

For cells containing a free surface, surface tension pressure normal to the free surface can be expressed as [38]

$$p_s = \gamma\kappa \tag{13}$$

where γ is the surface tension coefficient and κ is the free surface curvature given by

$$\kappa = -\left[\nabla \cdot \left(\frac{\vec{n}}{|\vec{n}|}\right)\right] = \frac{1}{|\vec{n}|}\left[\left(\frac{\vec{n}}{|\vec{n}|} \cdot \nabla\right)|\vec{n}| - (\nabla \cdot \vec{n})\right] \tag{14}$$

where $\vec{n}$ is a vector normal to the local free surface which equals the gradient of the VOF function

$$\vec{n} = \nabla F \tag{15}$$

The temperature-dependent Marangoni shear stress at the free surface in a direction tangential to the local free surface is given by [30]

$$\tau_{Ms} = \frac{\partial \gamma}{\partial T}\frac{\partial T}{\partial \vec{s}} \tag{16}$$

where $\vec{s}$ is a vector tangential to the local free surface.

The arc plasma shear stress is calculated at the free surface from the velocities of the arc plasma cells immediately next to the metal cells.

$$\tau_{ps} = \mu\frac{\partial \boldsymbol{V}}{\partial \vec{s}} \tag{17}$$

where μ is the viscosity of arc plasma.

The arc pressure at the metal surface is obtained from the computational result in the arc region. The surface forces are included by adding source terms to the momentum equations according to the CSF (continuum surface force) model [38–40]. Using F of the VOF function as the characteristic function, surface tension pressure, Marangoni shear stress, arc plasma shear stress, and arc pressure are all transformed to the localized body forces and added to the momentum transport equations as source terms at the boundary cells.

2.7. Energy terms at the arc plasma and metal interface

2.7.1. Plasma–anode interface

At the plasma–electrode interface, there exists an anode sheath region [8]. In this region, the mixture of plasma and metal vapor departs from LTE, thus it no longer complies with the model presented above. The thickness of this region is about 0.02 mm [8]. Since the sheath region is very thin, it is treated as a special interface to take into account the thermal effects on the electrode. The energy balance equation at the surface of the anode is modified to include an additional source term, S_a, as the following [13,21] for the metal region

$$S_{\mathrm{a}} = \frac{k_{\mathrm{eff}}(T_{\mathrm{arc}} - T_{\mathrm{a}})}{\delta} + J_{\mathrm{a}}\phi_{\mathrm{w}} - \varepsilon k_{\mathrm{b}} T_{\mathrm{a}}^4 - q_{\mathrm{ev}} H_{\mathrm{ev}} \tag{18}$$

The first term on the right-hand side of Eq. (18) is the contribution due to thermal conduction from the plasma to the anode. The symbol k_{eff} represents the thermal conductivity taken as the harmonic mean of the thermal conductivities of the arc plasma and the anode material. δ is the length of the anode sheath region, which is taken as 0.1 mm, the maximum experimentally observed thickness of the anode fall region [41]. T_{arc} is chosen to be the temperature of the first gas plasma cell along the normal direction, and T_{a} to be the temperature of the first metal cell along the normal direction at the local point. The second term represents the electron heating associated with the work function of the anode material. J_{a} is the square root of J_{r}^2 and J_{z}^2 and ϕ_{w} is the work function of the anode material. The third term is black body radiation loss from the anode surface. The final term is the heat loss due to the evaporation of electrode materials. ε is the emissivity of the surface and k_{b} is the Stefan–Boltzmann constant. q_{ev} is the mass rate of evaporation of metal vapor from the droplet, and H_{ev} is the latent heat of vaporization. For metal such as steel, q_{ev} can be written as [39]

$$\log(q_{\mathrm{ev}}) = A_v + \log P_{\mathrm{atm}} - 0.5 \log T \tag{19}$$

$$\log P_{\mathrm{atm}} = 6.121 - \frac{18836}{T} \tag{20}$$

At the arc–anode interface, the energy equation for the plasma only considers the cooling effects through conduction and the source term, S_{ap}, is given

$$S_{\mathrm{ap}} = -\frac{k_{\mathrm{eff}}(T_{\mathrm{arc}} - T_{\mathrm{a}})}{\delta} \tag{21}$$

2.7.2. Plasma–cathode interface

Similar to the anode region, there exists a cathode sheath region between the plasma and the cathode. However, the physics of the cathode sheath and the energy balance at the nonthermionic cathode for GMAW are not well understood [19–24,36]. The thermal effect due to the cathode sheath has been omitted in many models and reasonable results were obtained [8,20–24]. Thus, the energy balance equation at the cathode surface will only have the conduction, radiation, and evaporation terms

$$S_{\mathrm{c}} = \frac{k_{\mathrm{eff}}(T_{\mathrm{arc}} - T_{\mathrm{c}})}{\delta} - q_{\mathrm{ev}} H_{\mathrm{ev}} - \varepsilon k_{\mathrm{b}} T_{\mathrm{c}}^4 \tag{22}$$

where k_{eff} is the effective thermal conductivity at the arc–cathode surface taken as the harmonic mean of the thermal conductivities of the arc plasma and the cathode material. δ is the length of the cathode and is taken as 0.1 mm. T_{c} is the cathode surface temperature. And the heat loss from the plasma at the cathode surface is

$$S_{\mathrm{cp}} = -\frac{k_{\mathrm{eff}}(T_{\mathrm{arc}} - T_{\mathrm{c}})}{\delta} \tag{23}$$

2.8. Boundary conditions

2.8.1. External boundary conditions

The calculation domain, as shown in Fig. 1, is ABCDEFGA. Only half of the entire physical domain is calculated due to the cylindrical symmetry along the centerline AG. The corresponding external boundary conditions for the entire domain are listed in Table 1. Symmetrical boundary conditions are used along the centerline AG. The wire feed rate is incorporated through a boundary condition on v along AB. The imposed shielding gas flow is set through a boundary condition on v along BC. For the inflow of gas from the nozzle, the radial velocity component is omitted and the axial velocity component is determined from the formula for pipe flow as shown in the following [42]:

$$v(r) = \frac{2Q}{\pi} \frac{\left\{R_{\mathrm{n}}^2 - r^2 + (R_{\mathrm{n}}^2 - R_{\mathrm{w}}^2)\frac{\ln(r/R_{\mathrm{n}})}{\ln(R_{\mathrm{n}}/R_{\mathrm{w}})}\right\}}{\left\{R_{\mathrm{n}}^4 - R_{\mathrm{w}}^4 + \frac{(R_{\mathrm{n}}^2 - R_{\mathrm{w}}^2)^2}{\ln(R_{\mathrm{n}}/R_{\mathrm{w}})}\right\}} + V_{\mathrm{w}} \frac{\ln\frac{R_{\mathrm{n}}}{r}}{\ln\frac{R_{\mathrm{n}}}{R_{\mathrm{w}}}} \tag{24}$$

where Q is the inflow rate of the shielding gas, R_{w} is the radius of the electrode, R_{n} is the internal radius of the shielding gas nozzle, and V_{w} is the wire feed rate. A constant mass flow boundary condition is used for the open boundaries CD and DE.

The temperature boundaries along AD, DE, and EG are determined by the ambient condition, which is set as room temperature. Uniform current density is specified along AB as $J_z = -\sigma_{\mathrm{e}}\frac{\partial\phi}{\partial z} = \frac{I}{\pi R_{\mathrm{w}}^2}$. The voltage, ϕ, is set to zero at the bottom of the workpiece FG.

2.8.2. Internal boundary conditions

Within the computational domain, the moving surface of the electrode, droplet and weld pool forms the inner

Table 1
Boundary conditions on the outer boundaries

	AB	BC	CD	DE	EF	FG	GA
u	0	0	0	$\frac{\partial(\rho u)}{\partial r} = 0$	0	0	0
v	v_{w}	Eq. (24)	$\frac{\partial(\rho v)}{\partial z} = 0$	0	0	0	$\frac{\partial v}{\partial r} = 0$
h	$T = 300$ K	$T = 300$ K	$T = 300$ K	$T = 300$ K	$T = 300$ K	$T = 300$ K	$\frac{\partial T}{\partial r} = 0$
ϕ	$-\sigma\frac{\partial\phi}{\partial z} = \frac{I}{\pi R_{\mathrm{c}}^2}$	$\frac{\partial\phi}{\partial z} = 0$	$\frac{\partial\phi}{\partial z} = 0$	$\frac{\partial\phi}{\partial r} = 0$	$\phi = 0$	$\phi = 0$	$\frac{\partial\phi}{\partial r} = 0$

boundary for the arc region. VOF Eq. (12) is solved in the metal domain to track the moving free surface with free boundary conditions set at the metal free surface. Additional body force source terms are added to the momentum transport equations at the metal free surface to consider the effects of surface tension, Maragoni shear stress, arc plasma shear stress and arc pressure. Additional source terms described in Eqs. (18) and (22) are added to the energy equation for the special treatment of the anode sheath and the cathode sheath.

A fixed computational domain is used to solve the equations in the arc region. The metal region is used as the inner boundary for the arc region. As the velocity of the metal domain is much smaller than the velocity of the arc plasma, the metal region serves as an inner obstacle in the arc domain. The temperature at the metal free surface is considered as the temperature boundary for the arc domain.

3. Numerical considerations

In the present study, the transport phenomena in the arc plasma and the metal are calculated separately in the corresponding metal domain and arc domain, and the two domains are coupled through interfacial boundary conditions at each time step. The current distribution is greatly influenced by the temperature distribution in the arc column and the shape of the metal domain, but it is slightly influenced by the temperature distribution in the metal domain as the electrical conductivity of metal varies slightly with temperature. Therefore, the current continuity equation and its associated boundary conditions are solved in the entire domain, while other primary variables, including p, u, v, and T, are calculated separately in the metal domain and arc domain. The current continuity equation is iterated with the transport equations in the arc domain to obtain the current density distribution for both the arc domain and the metal domain. Iterations are required to assure convergence of each domain and then the boundary conditions are calculated from each domain for the coupling between the two domains.

For the metal domain, the method developed by Torrey et al. [37] was used to solve p, u, v, and T. This method is Eulerian and allows for an arbitrary number of segments of free surface with any reasonable shape. The basic procedure for advancing the solution through one time step, Δt, consists of three steps. First, at the beginning of the time step, explicit approximations to the momentum Eqs. (2) and (3) are used to find provisional values of the new time velocities. Second, an iterative procedure is used to solve for the advanced time pressure and velocity fields that satisfy Eq. (1) to within a convergence criterion at the new time. Third, the energy equation is solved.

For the arc plasma domain, a fully implicit formulation is used for the time-dependent terms, and the combined convection/diffusion coefficients are evaluated using an upwind scheme. The SIMPLE algorithm [43] is applied to solve the momentum and mass continuity equations to obtain the velocity field. At each time step, the current continuity equation is solved first, based on the updated parameters. The new distributions of current density and electromagnetic force are then calculated for the momentum and energy equations. The momentum equations and the mass continuity equation are then solved in the iteration process to obtain pressure and velocity. The energy equation is solved to get the new temperature distribution. Next, the temperature-dependent parameters are updated, and the program goes back to the first step to calculate the current continuity equation. This process is repeated for each time step until the convergence criteria are satisfied.

The governing differential equations (Eqs. (1)–(5) and (12)) and all related supplemental and boundary conditions are solved through the following iterative scheme:

1. At $t = 0$, the electrode is set up at an initial position and initial temperature distribution is given to the metal domain. Based on the initial fixed metal domain and temperature distribution, the initial distributions of temperature, velocity, pressure and current are obtained by solving the steady state equations in the arc domain (this procedure is similar to the steps from 5–7 for the steady state).
2. Surface tension, Marangoni shear stress, electromagnetic force, plasma shear stress and arc pressure are calculated, and other associated boundary conditions are evaluated for the metal domain.
3. Eqs. (1)–(4) are solved iteratively to obtain pressure, velocity and temperature in the metal domain.
4. Eq. (12) is solved to obtain the new free surface profile for the metal domain. The physical properties in the mesh cells and the boundary conditions within the computing domain are updated.
5. The current continuity equation (5) is solved in the whole domain with updated parameters. Current density and electromagnetic force are calculated.
6. Eqs. (1)–(3) and the associated boundary conditions are solved iteratively to get the velocity and pressure distributions of the arc plasma. When solving these equations, the electrode, droplet and the workpiece are treated as fixed inner obstacles.
7. Energy equation (4) is solved in the arc domain to get the new temperature distribution. Thermal physical properties of the arc plasma are updated. From here, the iteration goes back to step 5 to repeat the process for new distribution of current density, velocity, pressure, and temperature, until convergence criteria are satisfied.
8. Advance to the next time step and back to step 2 until the desired time is reached.

A non-uniform grid point system is employed with finer grid sizes near both the cathode and anode regions. The mesh sizes near the anode and cathode center are set as 0.01 cm. The calculation domain is half of the cylinder of

5.0 cm radius and 3.05 cm in length. Time step size is set as 5×10^{-6} s. Various grid sizes and time step sizes were employed to assure consistent computational results. The final grid and time-step sizes used in the present study can be considered as the compromised values between computational time and accuracy.

4. Results and discussion

The electrode is mild steel with a 0.16 cm diameter. The workpiece is also a mild steel disk with a 3 cm diameter and a 0.5 cm thickness. The current is set to be constant at 220 Å. The imposed external shielding gas flows out of a gas nozzle with a 1.91 cm inner diameter at a rate of 24 l/min. The contact tube is set flush with the bottom of the gas nozzle and is 2.54 cm above the workpiece. The initial arc length is set as 0.8 cm. The wire feed rate is 4.5 cm/s. The welding conditions are listed in Table 2. The temperature-dependent radiation loss term (S_R) in Eq. (4) and temperature-dependent material properties of argon, including density, specific heat, viscosity, electrical conductivity, and thermal conductivity, are taken from [36] and drawn in Fig. 2. The thermophysical properties of the solid and liquid mild steel are taken from [31], and are listed in Table 3 with other parameters used in the computation.

Fig. 3(a) through (c), respectively, show the distributions of temperature, arc plasma velocity, and electrical potential at $t = 100$ ms. The shape of the electrode and workpiece are marked with thick lines. From the temperature contours in the plasma in Fig. 3(a), it can be seen that the arc has a bell-shaped envelope, which covers the droplet and expands as it approaches the workpiece. This expansion cools the plasma and forms a high temperature cone underneath the droplet. The maximum temperature of the plasma is found to be 19300 K on the axis near the bottom of the droplet. The corresponding velocity distribution in Fig. 3(b) shows a strong downward arc plasma flow underneath the droplet. From the streamline, it can be clearly seen that shielding gas flows down from the gas nozzle along the electrode surface and then is drawn to the electrode around the electrode tip. The ionized shielding gas around the electrode tip is pinched by the radially inward and axially downward electromagnetic force toward the workpiece. The corresponding electromagnetic force in the arc column is shown in Fig. 4(b). When the plasma flow reaches the workpiece, the axial downward momentum is changed to the radial outward momentum and the plasma flows outward in the radial direction. The maximum axial velocity in the arc column is found to be 230 m/s on the axis.

Table 2
Welding conditions

Nomenclature	Value (unit)
Shielding gas	Argon
Shielding gas flow rate	23 (L min^{-1})
Internal diameter of shielding gas nozzle	19.1 (mm)
Welding current	220 (A)
Electrode diameter	1.6 (mm)
Contact tube to workpiece length	25.4 (mm)
Initial arc length	8.0 (mm)
Workpiece thickness	5.0 (mm)
Diameter of workpiece	30.0 (mm)
Wire feed speed	4.5 (cm s^{-1})
Welding time	1 (s)

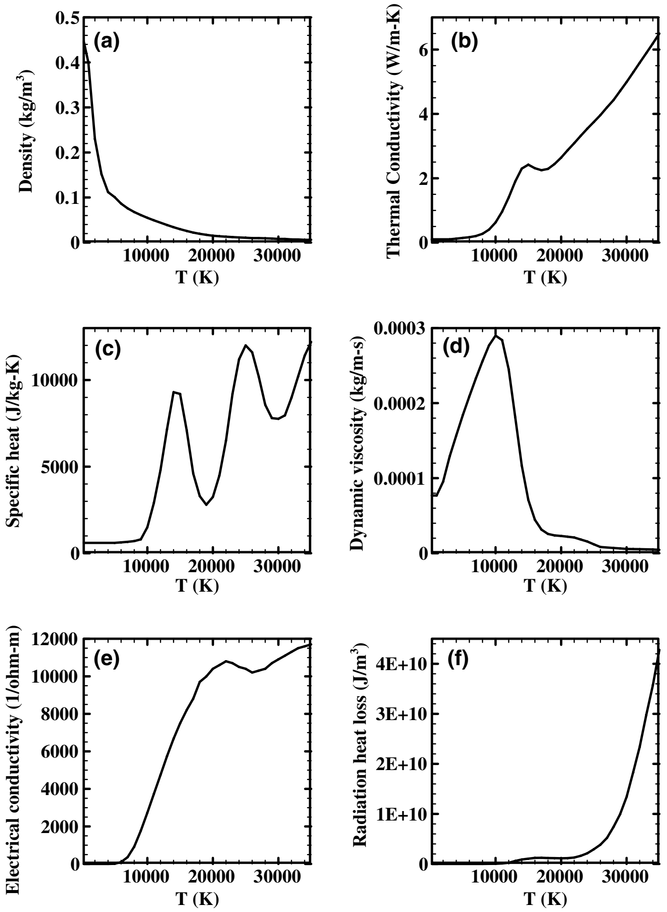

Fig. 2. Temperature-dependent material properties of argon and the volume radiation heat loss taken from [36].

Fig. 3(c) shows the corresponding electrical potential distribution at $t = 100$ ms. There are two distinct regions where dense electrical potential contours are observed. One is around the electrode with upside contour and another is near the cathode with downside contour. The gradient of the electrical potential is the current density. The electrical potential contours are denser, where the current density is higher. The upside contour shape shows current diverges from the center and the downside contour shape shows current converges to the center. From the corresponding current density distribution in Fig. 4(a), it is more clearly seen that current diverges from the electrode tip and converges at the cathode in the workpiece. The current flow pattern determines the inward and downward electromagnetic force around the droplet and the inward and upward electromagnetic force at the workpiece, as

Table 3
Thermophysical properties of mild steel and other parameters

Nomenclature	Symbol	Value (unit)
Constant in Eq. (19)	A_v	2.52
Specific heat of solid phase	c_s	700 (J kg^{-1} K^{-1})
Specific heat of liquid phase	c_l	780 (J kg^{-1} K^{-1})
Thermal conductivity of solid phase	k_s	22 (W m^{-1} K^{-1})
Thermal conductivity of liquid phase	k_l	22 (W m^{-1} K^{-1})
Density of solid phase	ρ_s	7200 (kg m^{-3})
Density of liquid phase	ρ_l	7200 (kg m^{-3})
Thermal expansion coefficient	β_T	4.95×10^{-5} (K^{-1})
Radiation emissivity	ε	0.4
Dynamic viscosity	μ_l	0.006 (kg m^{-1} s^{-1})
Latent heat of fusion	H	2.47×10^5 (J kg^{-1})
Latent heat of vaporization	H_{ev}	7.34×10^6 (J kg^{-1})
Solidus temperature	T_s	1750 (K)
Liquidus temperature	T_l	1800 (K)
Ambient temperature	T_∞	300 (K)
Vaporization temperature	T_{ev}	3080 (K)
Surface tension coefficient	γ	1.2 (N m^{-1})
Surface tension temperature gradient	$\partial\gamma/\partial T$	10^{-4} (N m^{-1} K^{-1})
Work function	ϕ_w	4.3 V
Electrical conductivity	σ_e	7.7×10^5 (Ω^{-1} m^{-1})

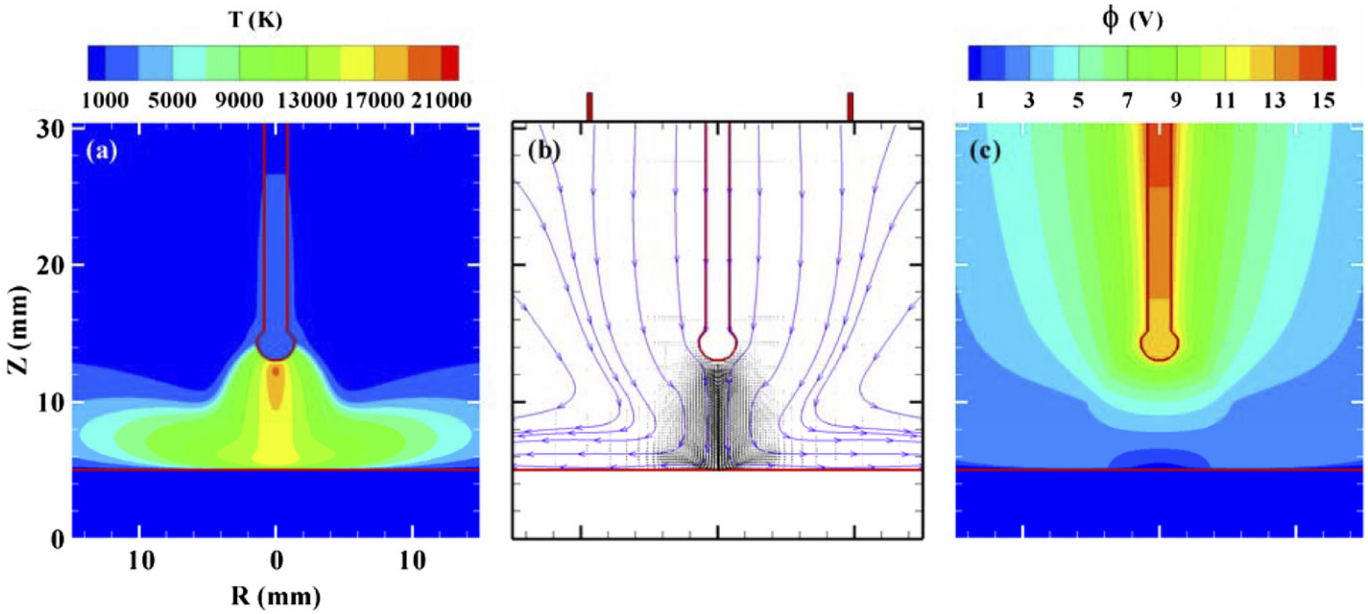

Fig. 3. Temperature, arc plasma velocity and electrical potential distributions at $t = 100$ ms. (a) temperature distribution; (b) velocity distribution; (c) electrical potential distribution.

shown in Fig. 4(b). From the streamlines shown in Fig. 4(a), it also can be seen that current is mainly confined in the arc column and very little amount of current is flowing outside the hot arc plasma column. Outside the high temperature arc column, the temperature of the arc plasma is low and thus the electrical conductivity is low. Note in order to increase the readability of flow direction, only a quarter of the grid nodes are used in Fig. 4(b).

The corresponding arc pressure contours at $t = 100$ ms are shown in Fig. 5(a), which shows two high pressure regions. One is underneath the droplet with a maximum of 800 Pa above the ambient pressure, and the other is near the cathode with a maximum of 600 Pa above the ambient pressure. The high pressure underneath the droplet is caused by the pinch effect of the electromagnetic force, which draws arc plasma flow underneath the droplet. The pressure increase near the cathode is due to the stagnation of the plasma flow impinging onto the workpiece. The arc pressure and shear stress versus the radial distance from the center of the workpiece at the workpiece surface are drawn in Fig. 5(b). The arc pressure has a Gaussian distribution, which only has high value in a small area near the cathode center and then decreases dramatically when it is away from the cathode center. Quite differently, the plasma shear

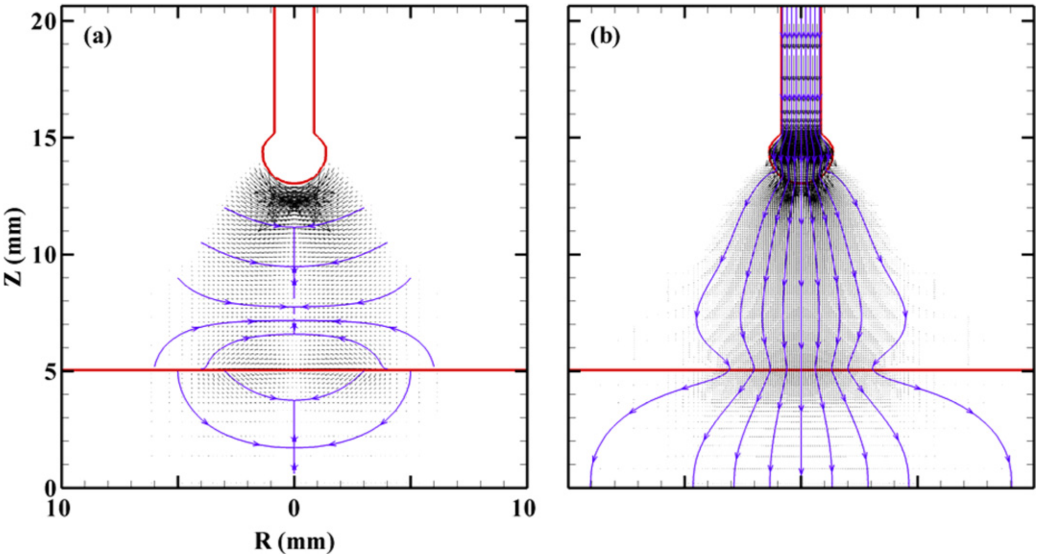

Fig. 4. Current and electromagnetic force distributions at $t = 100$ ms. (a) Current distribution; (b) electromagnetic force.

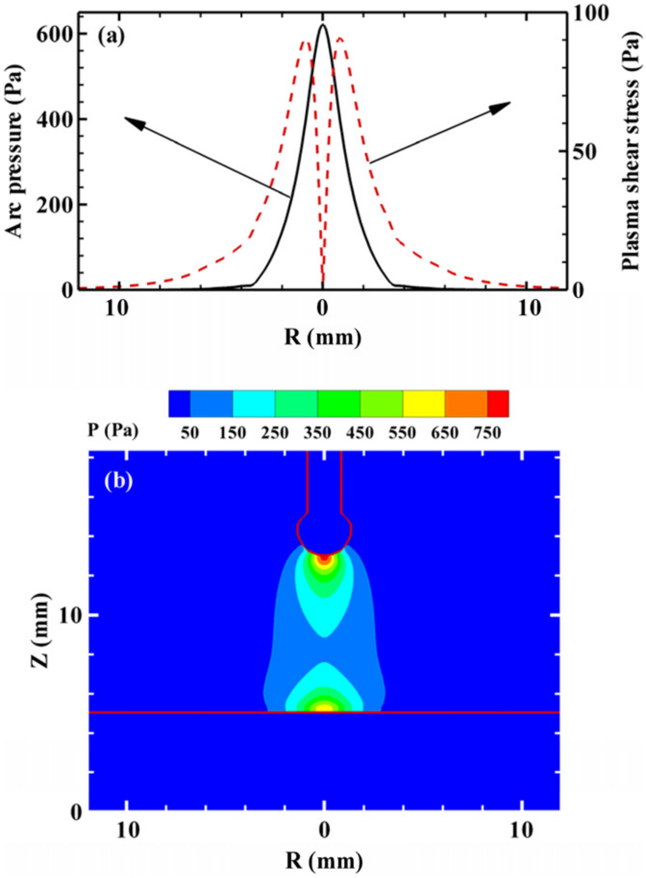

Fig. 5. Arc pressure and plasma shear stress distributions at $t = 100$ ms. (a) Pressure distribution in the arc plasma; (b) Arc pressure and plasma shear stress distribution at the workpiece surface.

stress has its maximum value at a certain distance away from the cathode center, which shows a trend to increase first and then decrease with the increase of the radial distance from the cathode center.

After the droplet is detached from the electrode, new arc plasma is struck between the electrode tip and the top surface of the detached droplet. During the process of the detached droplet being transferred to the workpiece, the existence of the moving droplet greatly distorts the arc shape. Figs. 6–9 show the distributions of temperature, current, plasma velocity, and plasma pressure at different instants. In order to increase the readability of flow direction, only a quarter of the grid nodes were used in Figs. 6–9. From the temperature contour and velocity distribution, it can be seen that arc plasma flows around the moving droplet. The high temperature and high velocity arc column is limited to the region between the electrode tip and the top of the detached droplet. The arc plasma temperature underneath the moving droplet decreases continuously after the droplet is detached from the electrode. The high velocity plasma flow induced by the pinch effect of the electromagnetic force underneath the moving droplet also subsides and vortices form underneath the droplet when it moves down to the workpiece. The phenomena are different from the simulation results of Zhu et al. [25], which reports a high temperature region underneath both the electrode tip and the moving droplet. However, these phenomena are supported by the experimental results of Jones et al. [26–31], which has shown that arc plasma tended to flow around the detached droplet and no high temperature zone underneath the detached droplet was observed.

From the current distribution in Fig. 6, it can be seen that current also flows around the detached droplet. Only a small amount of current flows through the detached droplet, except at $t = 118$ ms, when the droplet has just been detached and the temperature underneath the droplet is still relatively high. When the detached droplet moves farther away from the electrode tip in the cases of $t = 123$–133 ms, more current flows around the detached droplet. The arc plasma temperature quickly decreases

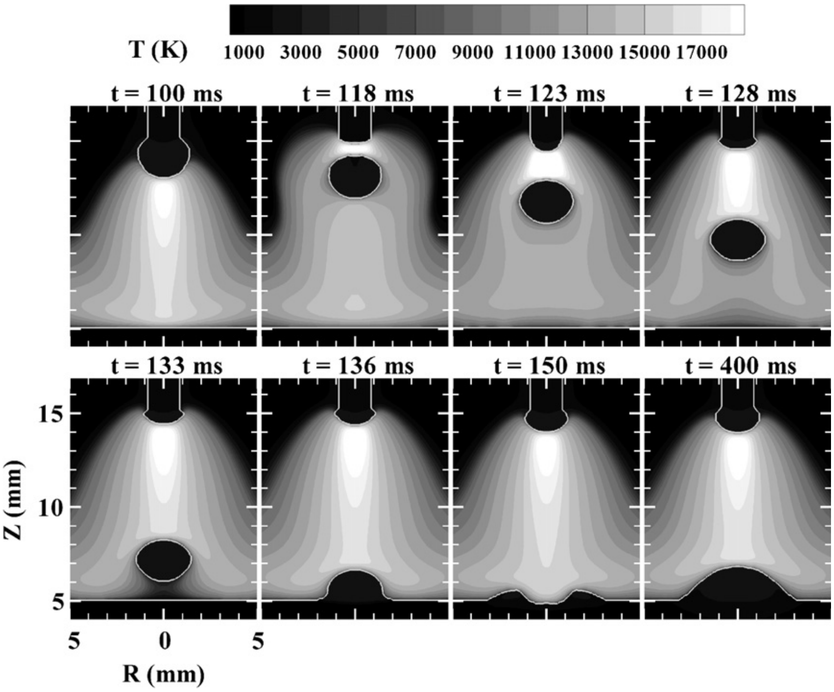

Fig. 6. Temperature distribution at different instants to show the influences of the detached droplet and the deformed weld pool on the arc plasma distribution.

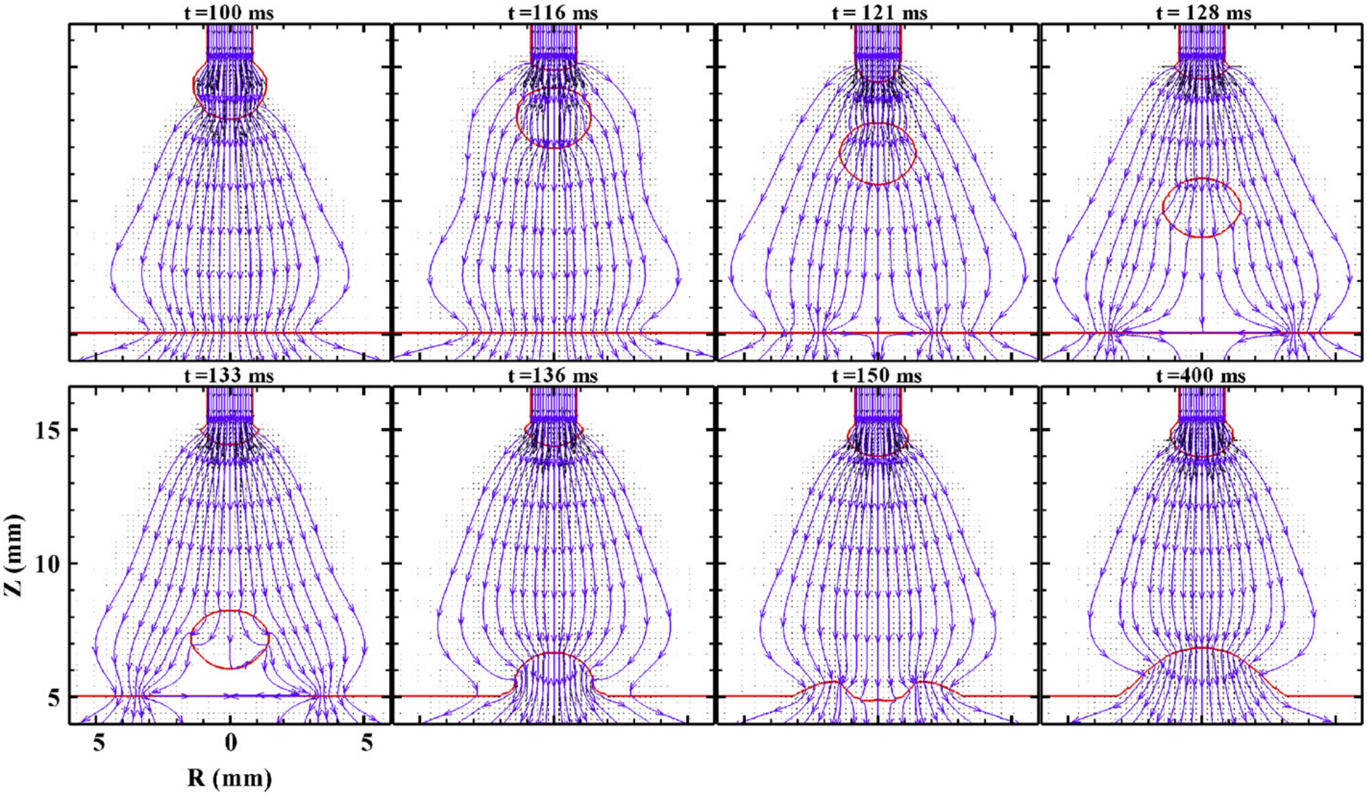

Fig. 7. The corresponding current distributions for the cases shown in Fig. 6.

when current flow decreases underneath the detached droplet due to the high radiation loss and low capacity of the plasma. The lower plasma temperature underneath the detached droplet further reduces the current flow in the plasma, and hence the plasma temperature continues to drop. At the surface of the workpiece, the current bypassed

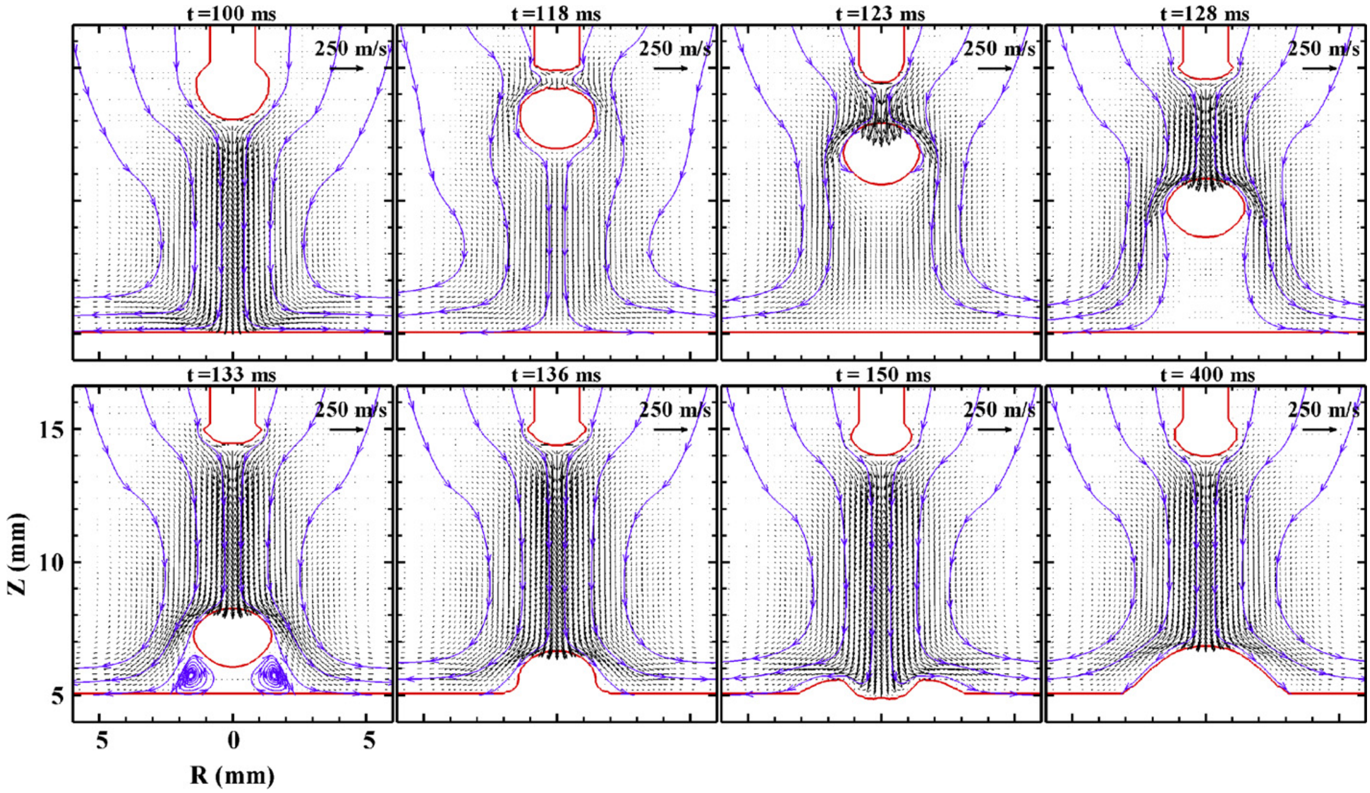

Fig. 8. The corresponding velocity distributions in the arc plasma for the cases shown in Fig. 6.

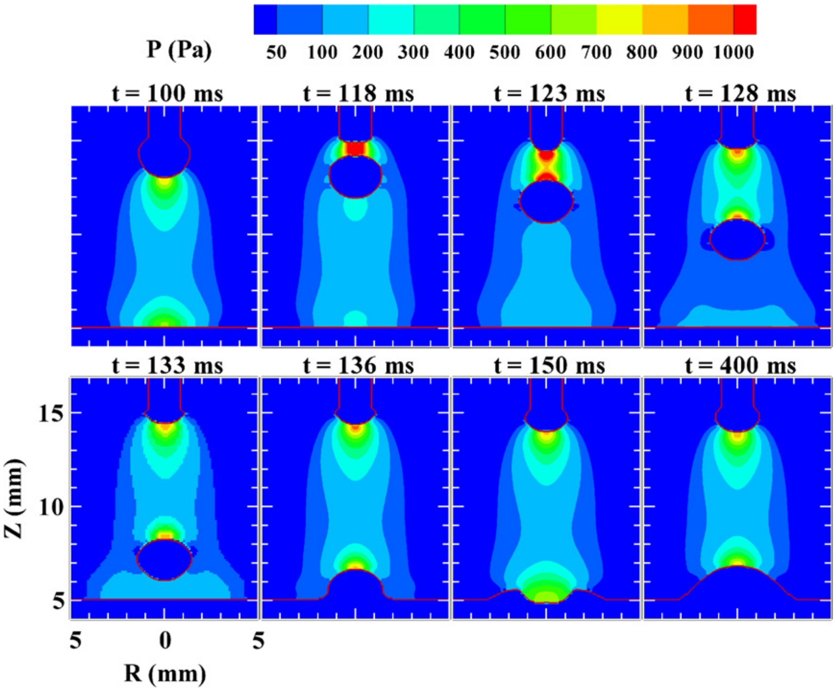

Fig. 9. The corresponding pressure distributions in the arc plasma for the cases shown in Fig. 6.

around the detached droplet tends to converge at a place other than the spot directly underneath the droplet. As a cylindrical system is used in this calculation, a ring of cathode spot, rather than a small continuous area, is predicted for the instants when a detached droplet is stuck between the electrode and the workpiece. In the practical welding process, the current may converge to some small projected area other than symmetrically around the workpiece. The

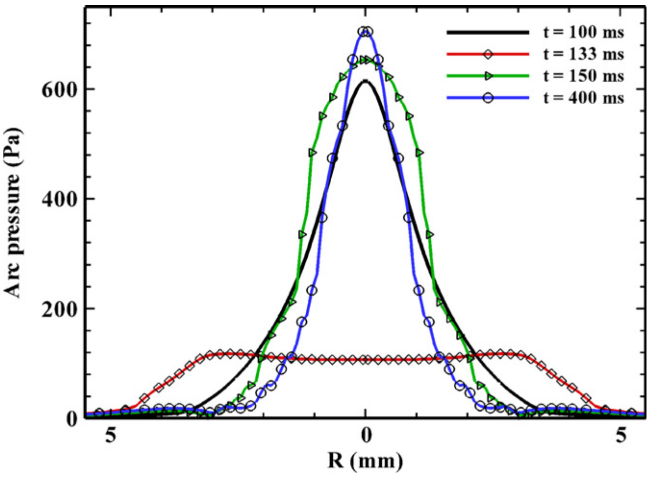

Fig. 10. Arc pressure distributions along the radial direction at the workpiece surface.

existence of the detached droplet also dramatically changes the arc pressure distribution underneath the droplet, as shown in Fig. 9. The arc pressure at the tip of the electrode and at the upper surface of the droplet is mainly influenced by the shapes of the electrode tip and the position of the detached droplet. After the droplet is detached, a high arc pressure forms between the electrode tip and the upper surface of the moving droplet. The high arc pressure, which was under the droplet before it was detached, decreases rapidly. The stagnation pressure underneath the droplet at the center of the workpiece also decreases rapidly. The pressure difference between the upper and lower surfaces of the droplet helps to push the detached droplet down to the workpiece.

In GTAW welding, the cathode tip shape greatly influences the welding results because the cathode tip shape determines the current flow into the cathode tip. The more projected the cathode, the more concentrated is the current flow and thus the more concentrated arc plasma with higher temperature and higher arc pressure. In the same way, the current distribution at the cathode in GMAW, which is the weld pool, is greatly influenced by the weld pool surface shape. The temperature, current, arc plasma velocity and arc pressure distributions from $t = 136$ ms to $t = 400$ ms in Figs. 6–9 show the influence of the weld pool shape on the arc plasma. The current tends to converge on the projected area at the workpiece, which may be at the workpiece center as in the cases of both $t = 136$ ms and $t = 400$ ms or not at the center as that of $t = 150$ ms. The temperature distribution and the pressure distribution at the deformed weld pool surface from $t = 136$ ms to $t = 400$ ms in Figs. 6 and 9, also show a different pattern from those at the flat weld pool surface.

In the existing models of simulating the weld pool dynamics, the arc pressure distribution at the center of the workpiece surface was assumed to be a Gaussian distribution with a fixed amplitude and distribution radius. However, the arc pressure distribution at the workpiece surface changes dramatically during the welding process. Fig. 10 shows the arc pressure along the weld pool surface at different instants. As shown in Fig. 10, the arc pressure spreads to a wide surface with lower amplitude when there is a detached droplet stuck between the electrode tip and the workpiece at $t = 133$ ms. The deformed weld pool surface greatly affects the arc pressure distribution at the weld pool surface. The depressed weld pool surface at $t = 150$ ms helps to distribute the arc pressure more uniformly at the weld pool center and reduce the arc pressure where it is away from the center. The arc pressure distribution is concentrated at the weld pool center with a projected weld pool surface at $t = 400$ ms. A small weld pool is simulated with a short simulated welding time, while much higher weld pool deformations can be found in a large weld pool with long welding time. The highly deformed weld pool surface will more dramatically change the arc distribution at the weld pool surface. Thus, it shows that the assumed Gaussian distribution of the arc pressure cannot reflect the real arc pressure distribution at the weld pool surface. Similarly, the current distribution and heat flux cannot be assumed as Gaussian distributions with fixed amplitude and fixed distribution radius. The influences of the moving droplet and the deformed weld pool surface on the current and temperature distributions at the weld pool surface have been explained earlier in this section. The heat flux to the weld pool surface is determined by the current and temperature distribution at the weld pool surface. Thus, a unified model that simulates the coupling of the arc and metal domain is needed to provide better boundary conditions at the metal surface for both domains.

5. Conclusions

A unified model has been developed to simulate the transport phenomena occurring during a gas metal arc welding process. An interactive coupling between the arc plasma; the melting of the electrode; the droplet generation, detachment, transfer, and impingement onto the workpiece; and weld pool dynamics were considered. The heat transfer and fluid flow in the arc column were studied based on the transient distributions of current, temperature, velocity, and pressure in the arc plasma, droplet, and weld pool calculated in the unified model. The moving droplet stuck between the electrode tip and the workpiece and the deformed weld pool were found to distort the arc flow and affect the current, temperature, velocity, and pressure distribution in the arc column. The assumed Gaussian distributions of the arc pressure, current and heat flux at the weld pool surface in the traditional models were shown not to be representative of the real distributions in the welding process.

Acknowledgement

This work was partially supported by GM R&D Center which is gratefully acknowledged.

References

[1] J. Mckelliget, J. Szekely, Heat transfer and fluid flow in the welding arc, Metall. Trans. 17A (1986) 1139–1148.

[2] R.T.C. Choo, J. Szekely, R.C. Westhoff, On the calculation of the free surface temperature of gas-tungsten-arc weld pools from first principles: Part I. Modeling the welding arc, Metall. Trans. 23B (1992) 357–369.

[3] M. Goodarzi, R. Choo, J.M. Toguri, The effect of the cathode tip angle on the GTAW arc and weld pool: I. Mathematical model of the arc, J. Phys. D: Appl. Phys. 30 (1997) 2744–2756.

[4] H.G. Fan, S.-J. Na, Y.W. Shi, Mathematical model of arc in pulsed current gas tungsten arc welding, J. Phys. D: Appl. Phys. 30 (1998) 94–102.

[5] H.G. Fan, Y.W. Shi, Numerical simulation of the arc pressure in gas tungsten arc welding, J. Mater. Process. Tech. 61 (1996) 302–308.

[6] P. Zhu, J.J. Lowke, R. Morrow, A unified theory of free burning arcs, cathode sheaths and cathodes, J. Phys. D: Appl. Phys. 25 (1992) 1221–1230.

[7] J.J. Lowke, R. Morrow, J. Haidar, A simplified unified theory of arcs and their electrodes, J. Phys. D: Appl. Phys. 30 (1997) 2033–2042.

[8] J.J. Lowke, P. Kovitya, H.P. Schmidt, Theory of free-burning arc columns including the influence of the cathode, J. Phys. D: Appl. Phys. 25 (1992) 1600–1606.

[9] P. Zhu, J.J. Jowke, R. Morrow, J. Haidar, Prediction of anode temperatures of free burning arcs, J. Phys. D: Appl. Phys. 28 (1995) 1369–1376.

[10] J. Haidar, Departures from local thermodynamic equilibrium in high-current free burning arcs in argon, J. Phys. D: Appl. Phys. 30 (1997) 2737–2743.

[11] L. Sansonnens, J. Haidar, J.J. Lowke, Prediction of properties of free burning arcs including effects of ambipolar diffusion, J. Phys. D: Appl. Phys. 33 (2000) 148–157.

[12] M. Tanaka, H. Terasaki, M. Ushio, J.J. Lowke, A unified numerical modeling of stationary tungsten-inert gas welding process, Metall. Trans. 33A (2002) 2002–2043.

[13] J. Haidar, A theoretical model for gas metal arc welding and gas tungsten arc welding. I, J. Appl. Phys. 84 (7) (1998) 3518–3529.

[14] R.J. Ducharme, P.D. Kapadia, J. Dowden, I.M. Richardson, M.F. Thornton, A mathematical model of TIG electric arcs operating in the hyperbaric range, J. Phys. D: Appl. Phys. 29 (1996) 2650–2658.

[15] J. Menart, J. Heberlein, E. Pfender, Theoretical radiative transport results for a free-burning arc using a line-by-line technique, J. Phys. D: Appl. Phys. 32 (1999) 55–63.

[16] J. Menart, S. Malik, L. Lin, Coupled radiative, flow and temperature-field analysis of a free-burning arc, J. Phys. D: Appl. Phys. 33 (2000) 257–269.

[17] H.P. Schmidt, G. Speckhofer, Experimental and theoretical investigation of high-pressure arcs-Part I: the cylindrical arc column (two-dimensional modeling), IEEE Trans. Plasma Sci. 24 (1996) 1229–1238.

[18] G. Speckhofer, H.P. Schmidt, Experimental and theoretical investigation of high-pressure arcs-Part II: the magnetically deflected arc (three-dimensional modeling), IEEE Trans. Plasma Sci. 24 (1996) 1239–1248.

[19] P.G. Jonsson, R.C. Westhoff, J. Szekely, Arc characteristics in gas-metal arc welding of aluminum using argon as the shielding gas, J. Appl. Phys. 74 (1993) 5997–6006.

[20] P. Zhu, M. Rados, S.W. Simpson, A theoretical study of gas metal arc welding system, Plasma Sources Sci. Technol. 4 (1995) 495–500.

[21] J. Haidar, J.J. Lowke, Predictions of metal droplet formation in arc welding, J. Phys. D: Appl. Phys. 29 (1996) 2951–2960.

[22] J. Haidar, An analysis of the formation of metal droplets in arc welding, J. Phys. D: Appl. Phys. 31 (1998) 1233–1244.

[23] J. Haidar, Prediction of metal droplet formation in gas metal arc welding. II, J. Appl. Phys. 84 (7) (1998) 3530–3540.

[24] J. Haidar, An analysis of heat transfer and fume production in gas metal arc welding. III, J. Appl. Phys. 85 (7) (1998) 3448–3459.

[25] F.L. Zhu, H.L. Tsai, S.P. Marin, P.C. Wang, A comprehensive model on the transport phenomena during gas metal arc welding process, Prog. Comput. Fluid Dyn. 4 (2) (2004) 99–117.

[26] H.G. Fan, R. Kovacevic, A unified model of transport phenomena in gas metal arc welding including electrode, arc plasma and molten pool, J. Phys. D: Appl. Phys. 37 (2004) 2531–2544.

[27] L.A. Jones, T.W. Eagar, J.H. Lang, Images of steel electrode in Ar–2%O_2 shielding during constant current gas metal arc welding, Welding J. (1998) 135s–141s.

[28] L.A. Jones, T.W. Eagar, J.H. Lang, Magnetic forces acting on molten drops in gas metal arc welding, J. Phys. D: Appl. Phys. 31 (1998) 93–106.

[29] L.A. Jones, T.W. Eagar, J.H. Lang, A dynamic model of drops detaching from a gas metal arc welding electrode, J. Phys. D: Appl. Phys. 31 (1998) 107–123.

[30] H.G. Fan, R. Kovacevic, Droplet formation, detachment, and impingement on the molten pool in gas metal arc welding, Metall. Trans. 30B (1999) 791–801.

[31] H.G. Fan, R. Kovacevic, Dynamic analysis of globular metal transfer in gas metal arc welding – a comparison of numerical and experimental results, J. Phys. D: Appl. Phys. 31 (1998) 2929–2941.

[32] Q.Z. Diao, H.L. Tsai, Modeling of solute redistribution in the mushy zone during solidification of aluminum-copper alloys, Metall. Trans. 24A (1993) 963–973.

[33] P.C. Carman, Fluid flow through granular beds, Trans. Inst. Chem. Engs. 15 (1937) 150–166.

[34] K. Kubo, R.D. Pehlke, Mathematical modeling of porosity formation in solidification, Metall. Trans. 16A (1985) 823–829.

[35] G.S. Beavers, E.M. Sparrow, Non-Darcy flow through fibrous porous media, J. Appl. Mech. 36 (1969) 711–714.

[36] J.F. Lancaster, The Physics of Welding, second ed., Oxford Pergamon, 1986.

[37] M.D. Torrey, L.D. Cloutman, R.C. Mjolsness, C.W. Hirt, NASA-VOF2D: A computer program for incompressible flows with free surfaces LA-10612-MS, Los Alamos National Laboratory, 1985.

[38] J.U. Brackbill, D.B. Kothe, C. Zemach, A continuum method for modeling surface tension, J. Comput. Phys. 100 (1992) 335–354.

[39] T. Zacharia, S.A. David, J.M. Vitek, Effect of evaporation and temperature-dependent material properties on weld pool development, Metall. Trans. 22B (1992) 233–241.

[40] A. Celic, G.G. Zilliac, Computational study of surface tension and wall adhesion effects on an oil film flow underneath an air boundary layer, Nasa Ames Research Center, 1997.

[41] W. Finkelnburg, S.M. Segal, The potential field in and around a gas discharge, and its influence on the discharge mechanism, Phys. Rev. Lett. 83 (1951) 582–585.

[42] R.A. Granger, Fluid mechanics, CBS College, New York, 1985 (Chapter 10).

[43] S.V. Patanka, Numerical heat transfer and fluid flow, McGraw-Hill, New York, 1980.